Title

Mathematical Modelling of Arctic Polygonal Tundra with Ecosys: 2. Microtopography Determines How CO2 and CH4 Exchange Responds to Changes in Temperature and Precipitation

Journal

Journal of Geophysical Research Biogeosciences, 122(12)

ISSN

2169-8953

Authors

Grant, RF
Mekonnen, ZA
Riley, WJ
et al.

Publication Date

2017-12-01

DOI

10.1002/2017jg004037

Peer reviewed

AGU PUBLICATIONS

JGR

Journal of Geophysical Research: Biogeosciences

RESEARCH ARTICLE
10.1002/2017JG004037

This article is a companion to Grant et al. (2017), https://doi.org/10.1002/2017JG004035.

Key Points:
- Topographic effects on CO_2 fluxes caused lower features to be net C sinks and higher features to be near C neutral
- Topographic effects on CH_4 fluxes caused lower features to be larger CH_4 sources and higher features to be smaller CH_4 sources
- Much of spatial and temporal variations in CO_2 and CH_4 fluxes were attributed in the model to topographic effects of water and snow movement

Correspondence to:
R. F. Grant,
rgrant@ualberta.ca

Citation:
Grant, R. F., Mekonnen, Z. A., Riley, W. J., Arora, B., & Torn, M. S. (2017). Mathematical modelling of arctic polygonal tundra with *ecosys*: 2. Microtopography determines how CO_2 and CH_4 exchange responds to changes in temperature and precipitation. *Journal of Geophysical Research: Biogeosciences*, *122*, 3174–3187. https://doi.org/10.1002/2017JG004037

Received 5 JUL 2017
Accepted 8 NOV 2017
Accepted article online 17 NOV 2017
Published online 20 DEC 2017

Mathematical Modelling of Arctic Polygonal Tundra with *Ecosys*: 2. Microtopography Determines How CO_2 and CH_4 Exchange Responds to Changes in Temperature and Precipitation

R. F. Grant[1], Z. A. Mekonnen[2], W. J. Riley[2], B. Arora[2], and M. S. Torn[2]

[1]Department of Renewable Resources, University of Alberta, Edmonton, Alberta, Canada, [2]Earth Science Division, Lawrence Berkeley National Laboratory, Berkeley, CA, USA

Abstract Differences of surface elevation in arctic polygonal landforms cause spatial variation in soil water contents (θ), active layer depths (ALD), and thereby in CO_2 and CH_4 exchange. Here we test hypotheses in *ecosys* for topographic controls on CO_2 and CH_4 exchange in trough, rim, and center features of low- and flat-centered polygons (LCP and FCP) against chamber and eddy covariance (EC) measurements during 2013 at Barrow, Alaska. Larger CO_2 influxes and CH_4 effluxes were measured with chambers and modeled with *ecosys* in LCPs than in FCPs and in lower features (troughs) than in higher (rims) within LCPs and FCPs. Spatially aggregated CO_2 and CH_4 fluxes from *ecosys* were significantly correlated with EC flux measurements. Lower features were modeled as C sinks (52–56 g C m^{-2} yr^{-1}) and CH_4 sources (4–6 g C m^{-2} yr^{-1}), and higher features as near C neutral (−2–15 g C m^{-2} yr^{-1}) and CH_4 neutral (0.0–0.1 g C m^{-2} yr^{-1}). Much of the spatial and temporal variations in CO_2 and CH_4 fluxes were modeled from topographic effects on water and snow movement and thereby on θ, ALD, and soil O_2 concentrations. Model results forced with meteorological data from 1981 to 2015 indicated increasing net primary productivity in higher features and CH_4 emissions in some lower and higher features since 2008, attributed mostly to recent rises in precipitation. Small-scale variation in surface elevation causes large spatial variation of greenhouse gas (GHG) exchanges and therefore should be considered in estimates of GHG exchange in polygonal landscapes.

1. Introduction

Coastal arctic landscapes are characterized by small-scale spatial variation in surface elevations of features (troughs, rims, and centers) in polygonal landforms underlain by shallow water tables that form within shallow active layers over impermeable permafrost. This variation in surface elevation may cause large variation in soil water contents (θ) at small spatial scales due to topographic effects on water and snow movement.

Spatial variation in θ may cause spatial variation in biogeochemical processes, plant functional types (PFTs), and productivities, and hence in ecosystem carbon storage (Wainwright et al., 2015; Zona et al., 2011) and in CO_2 and CH_4 exchanges with the atmosphere (Vaughn et al., 2016). More rapid CO_2 emissions have been recorded from higher rims than from lower troughs and centers, likely because lower water tables improved aeration in higher landform features (Olivas et al., 2011; Zona et al., 2011). Consequently, lower lying features in arctic tundra may be CO_2 sinks while more elevated features may be CO_2 sources due to greater ecosystem respiration (R_e) and smaller gross primary productivity (GPP) in drier soils (Sjögersten et al., 2006).

More rapid CH_4 emissions have been recorded from troughs and centers than from rims of polygonal landforms (Vaughn et al., 2016), indicating poorer aeration in lower features with greater active layer depth (ALD) and smaller water table depth (Zona et al., 2009). These emissions may vary by up to 2–3 orders of magnitude among different features within these landforms (Morrissey & Livingston, 1992).

The small-scale variation in greenhouse gas (GHG) exchanges within tundra landforms under a common climate may exceed large-scale variation in GHG exchange among different tundra ecosystems under different climates (Sommerkorn, 2008). Therefore, it is important to represent relationships between landscape hydrology and GHG exchanges in ecosystem models used to study climate change impacts on permafrost-affected ecosystems, as impacts on GHG exchange will be mediated by those on tundra

hydrology. However, these relationships have not yet been fully implemented in models of arctic ecosystems so that spatial variation in GHG exchange among topographic features within tundra landforms has not been adequately simulated.

If this spatial variation is to be modeled mechanistically, relationships between hydrology and GHG exchanges must be modeled from the three-dimensional coupling of physical processes driving the transport and transformation of heat, water, solutes, and gases, including O_2, CO_2, and CH_4, with biological processes driving the oxidation-reduction reactions by which these solutes and gases are transformed in permafrost-affected soils. This coupling has been described in the terrestrial ecosystem model *ecosys* and tested against topographically driven variation in GHG exchange in arctic, boreal, temperate, and tropical wetlands (Dimitrov et al., 2011, 2014; Grant et al., 2012, 2015; Grant & Roulet, 2002; Mezbahuddin et al., 2014). In the accompanying paper (Grant et al., 2017), we tested hypotheses that topographic effects on water and snow movement determine spatial variation in θ and ALD through their effects on thermal conductivity among landform features (troughs, rims, and centers) of different polygonal landforms in a coastal arctic tundra. Here we test hypotheses that spatial variation in θ and ALD can explain that in CO_2 exchange and CH_4 emissions through effects of θ on soil aqueous O_2 concentrations ($[O_{2s}]$) and water potentials (ψ_s) among these same features.

In this paper we test and apply the model in low- and flat-centered polygonal landforms (LCP and FCP) at the Next-Generation Ecosystem Experiment (NGEE-Arctic; http://ngee-arctic.ornl.gov/) site in Barrow, AK, where observations of soil hydrological and thermal conditions, surface gas and energy exchanges, and plant productivity are available. This testing was intended to contribute toward a key objective of NGEE Arctic: to advance a robust predictive understanding of Earth's climate and environmental systems by delivering a process-rich ecosystem model, extending from bedrock to the top of the vegetative canopy/atmospheric interface, in which the evolution of Arctic ecosystems in a changing climate can be modeled.

2. Field Experiment

2.1. Site Description

The Barrow Experimental Observatory (BEO) is located ~6 km east of Barrow, AK (71.3°N, 156.5°W), at the northern tip of Alaska's Arctic coastal plain. Barrow has a maritime climate characterized by long, dry winters and short, moist, cool summers, with a mean annual air temperature of −12°C and mean annual precipitation of 106 mm. Continuous ice-rich permafrost extends to >400 m depth, overlain by a shallow active layer whose depth varies spatially and temporally from approximately 20 to 60 cm (Shiklomanov et al., 2010). The BEO is more fully described in Dafflon et al. (2016, 2017), Vaughn et al. (2016), and Wainwright et al. (2015).

2.2. Site Measurements

Feature-scale CO_2 and CH_4 fluxes were measured with transparent and opaque surface chambers in troughs, rims, and centers of different polygons including LCPs and FCPs on several dates during 2013 by Torn (2016). Landscape-scale CO_2 and CH_4 fluxes were measured with eddy covariance (EC) over a fetch area that consisted mostly of LCPs and FCPs during 2013 by Torn et al. (2016). Uncertainties in EC CO_2 flux measurements were calculated according to Billesbach (2011). Further information about measurement protocols is posted in the NGEE Arctic archives (http://ngee-arctic.ornl.gov/).

3. Model Experiment

3.1. Model Description

Key model equations and their parameterizations used to test the hypotheses in this study are described in Appendices A through H in the supporting information to this article (Table 1). These equations are cited with regard to key model processes in section 4. Reference to these equations in the supporting information is intended to provide insight into model behavior but is not required to understand model results. Of particular relevance to this study are equations for kinetics of microbial oxidation-reduction reactions driving heterotrophic respiration (R_h) in Appendix A: *Microbial C, N, and P Transformations*, and those driving CH_4 production and consumption in Appendix G: *CH_4 Production and Consumption*. All reactants and products of these transformations are coupled to algorithms for vertical and lateral convective-diffusive transfer in gaseous and aqueous phases in Appendix D: *Soil Water, Heat, Gas and Solute Fluxes*. Hydraulic processes driving

Table 1
List of Appendices in the Supporting Information

Appendix	Title	Equations
A	Microbial C, N and P Transformations	(A1)–(A39)
B	Soil-Plant Water Relations	(B1)–(B14)
C	Gross Primary Productivity, Autotrophic Respiration, Growth and Litterfall	(C1)–(C53)
D	Soil Water, Heat, Gas and Solute Fluxes	(D1)–(D21)
E	Solute Transformations	(E1)–(E57)
F	Symbiotic N_2 Fixation	(F1)–(F26)
G	CH_4 Production and Consumption	(G1)–(G27)
H	Inorganic N Transformations	(H1)–(H21)

soil-plant-atmosphere water transfer using coupled algorithms for hydraulically driven root water uptake with energy-driven canopy transpiration are presented in Appendix B: *Soil–Plant Water Relations*. Biological processes driving primary productivity and plant growth are given in Appendix C: *Gross Primary Productivity, Autotrophic Respiration, Growth and Litterfall*. These processes are further described in earlier modeling of CO_2 and CH_4 fluxes in tropical (Mezbahuddin et al., 2014), temperate (Dimitrov et al., 2011; Grant et al., 2012), boreal (Dimitrov et al., 2014; Grant & Roulet, 2002), and arctic (Grant et al., 2015) wetlands. All parameters in these algorithms are unchanged from those in these earlier studies.

3.2. Model Runs

We defined the *ecosys* computational domains from the polygon classification scheme of Wainwright et al. (2015), in which polygons of 5–20 m at BEO were resolved into different types based on surface elevations. The LCP landform was represented as a center 6 m in width and length, surrounded by a rim 1 m in width and 0.2 m in height above the center, which was surrounded in turn by a trough 1 m in width and 0.2 m in depth below the rim (Grant et al., 2017, Figure 1a). The trough and the center were connected through a 1 m breach in the rim, based on the observation of Dafflon et al. (2017) that LCP ridges are variable in height. The FCP landform was represented by features with the same dimensions, but the center was level with the rim (Grant et al., 2017, Figure 1b). The landform surfaces were thus 36% centers, 28% rims, and 36% troughs, similar to those derived from a high-resolution digital elevation model by Kumar et al. (2016). Other landforms such as high-centered polygons (HCP) were not represented at this stage of model testing, based on the findings of Wainwright et al. (2015) that 47% of the BEO landscape is occupied by FCPs, and most of the remainder by LCPs.

Soil profiles representing the key properties of the centers, rims, and troughs used in *ecosys* are given in Grant et al. (2017, Table 2). Measurements of these properties indicated greater variation within than among features with no consistent topographic effects on soil horizonation (Kumar et al., 2016). Therefore, soil properties in each feature were assumed to be the same at any depth relative to its surface so that differences in modeled hydrological and thermal conditions among features could be attributed solely to microtopographic effects.

Each grid cell in the modeled LCP and FCP was initialized with the same populations of sedge (200 m^{-2}) and moss (10^4 m^{-2}) (Grant et al., 2015) in the model year 1980. Both model polygons were run from 1980 to 2015 using gap-filled 1/2-hourly meteorological data (shortwave and longwave radiations, air temperature, relative humidity, wind speed, and precipitation) from 1 January 1981 to 15 June 2013 derived by Xu and Yuan (2016) from the Barrow, AK, station of NOAA/Earth System Laboratory, Global Monitoring Division (http://www.esrl.noaa.gov/gmd/obop/brw/), and NOAA's National Climate Data Center, and then using 1-hourly meteorological data recorded from 16 June 2013 to 31 December 2015 at BEO by Hinzman et al. (2016).

To check that equilibrium conditions were achieved during the model runs, another run was conducted for the LCP and FCP under repeating 1987 weather with mean annual temperature (MAT) and total precipitation (−12.6°C and 128 mm) that closely approximated long-term averages at Barrow. Equilibrium was indicated by nearly unchanging model output (e.g., fluxes change by $<$1% per year) during successive years under annually repeating weather, allowing variation in model output from the production model runs to be attributed to variation in the 1981–2015 weather sequence. This equilibrium was achieved by 5 years after initialization.

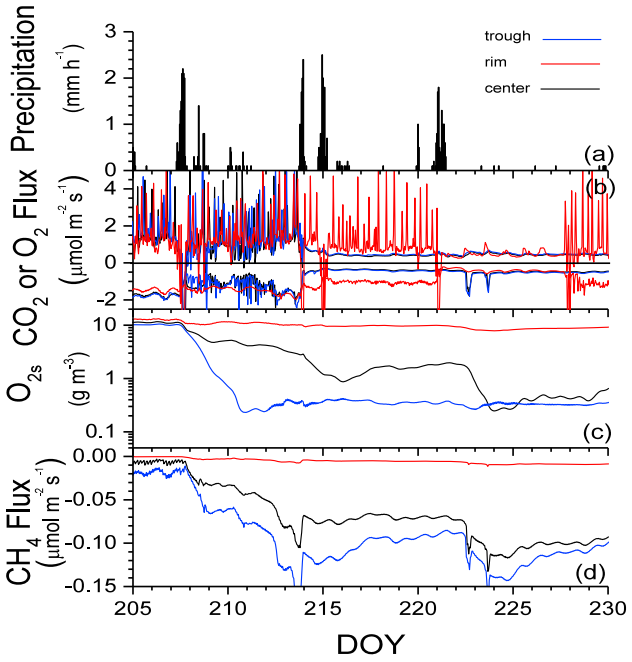

Figure 1. (a) Precipitation, (b) soil CO_2 and O_2 fluxes, (c) aqueous O_2 concentrations at 5 cm below the soil surface, and (d) CH_4 fluxes modeled at centers, rims, and troughs in a low-centered polygon at BEO from late July to mid-August 2013. In Figures 1b and 1d, positive values indicate O_2 influxes, while negative value indicate CO_2 or CH_4 effluxes.

During the model runs, variation in θ and ALD caused by topographic effects on snow and water movement (Grant et al., 2017) caused variation in gaseous and aqueous diffusivity (D17 and D20) and transfer (D16 and D19) that caused variation in solute and gas concentrations among features with different elevations. Variation in solute and gas concentrations caused variation in rates and energy yields of oxidation-reduction reactions conducted by different microbial and plant populations, including heterotrophic aerobes (bacteria and fungi (A11–A25) and facultative anaerobes (denitrifiers (H6–H10)) and obligate anaerobes (fermenters (G1–G6), acetotrophic methanogens (G7–G11), and nonsymbiotic diazotrophs (H3–H5)), autotrophic aerobes (nitrifiers (H11–H21) and methanotrophs (G18–G27)), anaerobes (hydrogenotrophic methanogens (G12–G17)), and roots and mycorrhizae (C13–C17), by which these solutes and gases were oxidized or reduced. Variations in rates and energy yields of these reactions were hypothesized to cause variation in soil CO_2 and CH_4 fluxes, as well as in ecosystem productivity, that would be consistent with those measured.

3.3. Model Tests

CO_2 and CH_4 fluxes modeled over troughs, centers, and rims in the LCP and FCP were tested against those measured with transparent flux chambers by Torn (2016) on six dates during 2013. Modeled fluxes were aggregated over all features in both the LCP and FCP and tested against EC measurements of CO_2 and CH_4 fluxes at BEO during 2013 by Torn et al. (2016). Chamber and EC fluxes were acquired from the NGEE Arctic archives (http://ngee-arctic.ornl.gov/). These tests were conducted by evaluating intercepts (a), slopes (b), correlations (R^2), and root-mean-square for differences (RMSD) from regressions of measured on modeled fluxes, representing variation in measured values not explained by the regression. A successful test would be indicated by values of a near zero, b near one, R^2 greater than that at $p = 0.001$, and RMSD similar to root-mean-square for error (RMSE) in measured values caused by measurement uncertainty, indicating that agreement between modeled and measured values was limited by uncertainty in measured values.

CO_2 and CH_4 fluxes modeled in troughs, rims, and centers of the LCP and FCP were also compared against measurements with opaque flux chambers by Torn (2016) on six dates during 2013. Biomass and LAI of sedge modeled on 3 August 2012 were compared with those measured on the same date for vascular species in troughs, rims, and centers of the LCP and FCP.

4. Results and Discussion

4.1. Spatial Variation in Soil CO_2 and CH_4 Fluxes Among Features Within Polygon Landforms

Surface gas exchange in rims, centers, and troughs was affected by spatial variation in modeled and measured θ caused by vertical and lateral water movement driven by elevation differences within LCP and FCP landforms (Grant et al., 2017, Figure 3). The modeled effects of θ on surface gas fluxes and $[O_{2s}]$ were examined during wetting and drying cycles in the LCP during July and August 2013 (Figure 1). Surface runoff and drainage following limited rainfall in early-mid July (before day of year (DOY) 207 in Figure 1a) allowed sufficient air-filled porosity (θ_a) to maintain relatively rapid O_2 influxes and CO_2 effluxes in all features (Figure 1b). However, following heavier rainfall on DOY 208, greater declines in θ_a and hence in O_2 influxes and CO_2 effluxes were modeled in poorly drained centers and troughs than in better drained rims (Figure 1b). Further rainfall on DOY 215 and 221 sharply reduced θ_a and hence O_2 influxes and CO_2 effluxes in rims (Figure 1b). Subsequent drying allowed θ_a and hence gas fluxes in rims to rise after DOY 228 while θ_a and hence gas fluxes remained small in troughs and centers (Figure 1b). Large atmospheric O_2 concentrations caused convective effects on gaseous O_2 influxes to be modeled with larger changes in θ_a during wetting from precipitation and drying from evapotranspiration, causing short-term temporal variation in O_2 influxes.

Table 2
Statistics From Regressions of CO_2 and CH_4 Fluxes Measured by Torn (2016) on Those Modeled by Ecosys in LCP and FCP Landforms at BEO During 2013

		a[a]	b[a]	R^2	RMSD[b]	RMSE[c]	n
Landform	μmol m^{-2} s^{-1}			μmol m^{-2} s^{-1}	μmol m^{-2} s^{-1}		
LCP	CO_2	−1.08	1.20	0.70*	1.15	1.07	18
	CH_4	−0.02	1.12	0.86*	0.012	0.047	18
FCP	CO_2	−0.54	1.46	0.88*	0.47	0.96	18
	CH_4	0.00	0.67	0.93*	0.005	0.008	18

[a]$Y = a + bX$ from regression of measured Y on simulated X. [b]RMSD from regression of measured Y on simulated X. [c]RMSE estimated from replication in measured values.
*Significant at $p < 0.001$.

More rapid O_2 influxes allowed greater $[O_{2s}]$ to be maintained in all features before the onset of heavier rains on DOY 208 (Figure 1c). Thereafter $[O_{2s}]$ modeled in troughs and centers declined with soil wetting, while those in rims remained near equilibrium with atmospheric concentrations. Declining $[O_{2s}]$ drove more rapid CH_4 emissions modeled in troughs and centers while greater $[O_{2s}]$ suppressed CH_4 emissions modeled in rims (Figure 1d).

4.2. Modeling Spatial Variation in Soil CO_2 and CH_4 Fluxes

Topographic effects on CO_2 emissions were modeled in *ecosys* through topographic effects of θ_a on gaseous convective-diffusive transfer (D16 and D17) and gaseous – aqueous dissolution (D14). These effects controlled $[O_{2s}]$ and thereby aerobic and anaerobic R_h. In higher features with drier soils and larger θ_a, more rapid O_2 transfers (A17) (Figure 1b) caused greater $[O_{2s}]$ (Figure 1c) and hence R_h (A14). More rapid R_h drove more rapid uptake of dissolved organic C (DOC) by aerobic heterotrophs (A21) that drove more rapid growth from large energy yields of O_2 reduction (A25). More rapid growth further increased heterotrophic biomass and hence R_h and thereby caused more rapid CO_2 emissions in higher than in lower features (Figure 1b) as observed experimentally by Zona et al. (2011).

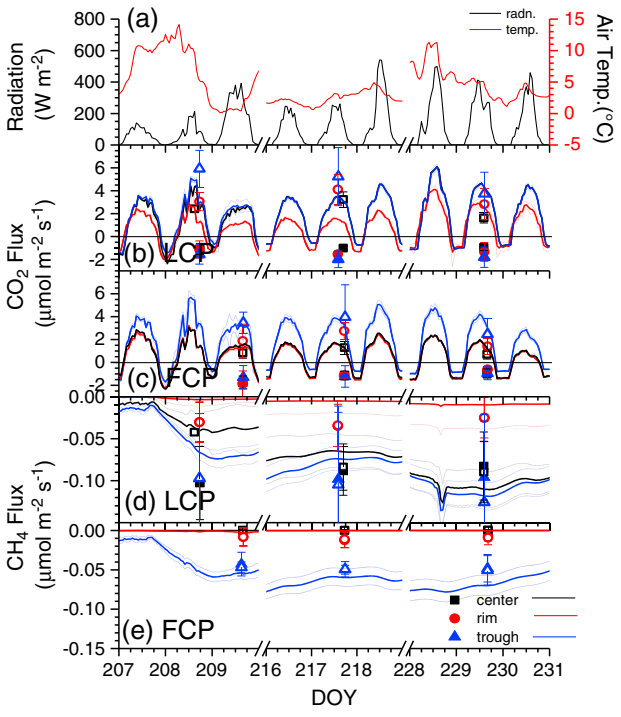

Figure 2. (a) Recorded radiation and temperature, (b) CO_2 fluxes, and (c) CH_4 fluxes modeled (lines) and measured with transparent (open symbols) and opaque (closed symbols) chambers at centers, rims, and troughs in low-centered polygons during three chamber measurement periods at BEO from late July to mid-August 2013. The lighter lines indicate standard deviations of values modeled in the grid cells of each feature. Measured fluxes from Torn (2016). For fluxes, positive values indicate influxes, while negative values indicate effluxes.

In lower features with wetter soils and smaller θ_a, slower transfer of O_2 (Figure 1b) caused declines in $[O_{2s}]$ (Figure 1c) and hence slower DOC uptake by aerobic heterotrophs, reducing competition for DOC uptake with fermenters not dependent on O_{2s} (G1). Consequent hastening of fermenter DOC uptake (G3) and hence R_h (G1) drove more rapid fermenter growth (G6). However, growth of fermenters under low $[O_{2s}]$ was slower than that of aerobic heterotrophs under high $[O_{2s}]$ because energy yield from reduction of DOC by fermenters was smaller than that from reduction of O_2 by aerobes (G4), causing slower CO_2 emission (Figure 1b).

In lower features, more rapid fermenter growth caused more rapid generation of fermentation products acetate and H_2 (G2) and hence more rapid acetotrophic and hydrogenotrophic methanogenesis (G7, G12), while lower $[O_{2s}]$ slowed methanotrophy (G18), thereby increasing CH_4 emissions (Figure 1d).

4.3. Spatial Variation in Ecosystem CO_2 and CH_4 Fluxes Among Features Within Polygon Landforms

Regressions of CO_2 fluxes measured by transparent flux chambers on CO_2 fluxes modeled at times corresponding to those of the measurements indicated that the model simulated most of the spatial and temporal variations in CO_2 influxes measured over all features in both the LCP and the FCP (R^2 = 0.7–0.9 in Table 2) although with some bias ($a < 0$, $b > 1$). This bias was caused by accurately estimating larger influxes measured in the middle of the growing season (Figures 2b

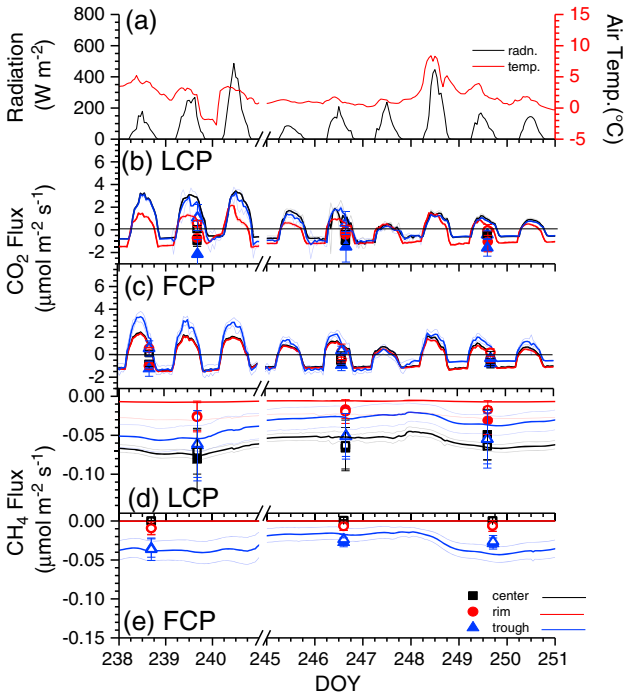

Figure 3. (a) Recorded radiation and temperature, (b) CO_2 fluxes, and (c) CH_4 fluxes modeled (lines) and measured with transparent (open symbols) and opaque (closed symbols) chambers at centers, rims, and troughs in low-centered polygons during three chamber measurement periods at BEO during late August and early September 2013. The lighter lines indicate standard deviations of values modeled in the grid cells of each feature. Measured fluxes from Torn (2016). For fluxes, positive values indicate influxes, while negative values indicate effluxes.

and 2c) but overestimating much smaller influxes measured toward the end of the growing season (Figures 3b and 3c). Values of RMSD from regressions of measured on modeled fluxes were comparable to those of RMSE from measured fluxes (Table 2). The model also simulated most of the spatial and temporal variations in CH_4 effluxes measured with opaque and transparent flux chambers in the LCP ($a \sim 0$, $b \sim 1$, $R^2 \sim 0.9$ in Table 2) but tended to underestimate the smaller effluxes measured in higher features ($b < 1.0$).

CO_2 effluxes measured with opaque flux chambers in the LCP during this period were greater in troughs than in rims and centers of the LCP, although differences among mean fluxes were less than measurement root mean squares for error (RMSE) (0.69 μmol m^{-2} s^{-1}) (Figure 2b). These chamber measurements included aboveground autotrophic respiration (R_a), and so were comparable with ecosystem CO_2 effluxes modeled during nights when solar radiation and hence GPP was near zero (Figure 2a). Ecosystem CO_2 effluxes modeled in the LCP were greater in rims than in troughs or centers (DOY 208–219 in Figures 1b and 2b) except when rims were wet (DOY 229–231 in Figures 1b and 2b). Ecosystem CO_2 effluxes modeled in the FCP were greater in rims and centers than in troughs (Figure 2c)

Greater CO_2 influxes were measured and modeled in LCP troughs than in LCP rims but CO_2 influxes modeled in centers were greater than those measured (Figure 2b). CO_2 influxes measured and modeled in the FCP were smaller than those in the LCP for all features, but particularly for centers, which were drier than those in the LCP (Grant et al., 2017, Figure 3). CO_2 effluxes measured and modeled for all features in the FCP remained similar to those in the LCP (Figure 2c versus Figure 2b).

In general, greater CO_2 influxes and smaller CO_2 effluxes were modeled in lower versus higher features in both landforms from late July to mid-August. During this period with long daylengths, modeled and measured CO_2 exchange indicated that lower features were large C sinks (net ecosystem productivity (NEP) greater than zero) while higher features were much smaller C sinks (NEP closer to zero).

Greater CH_4 effluxes were measured and modeled in LCP troughs and centers than in rims (Figure 2d). Smaller CH_4 effluxes were measured and modeled in the FCP than in the LCP (Figure 2e), particularly in FCP rims and centers, which were drier than those in the LCP (Grant et al., 2017, Figure 3).

CO_2 influxes and CH_4 effluxes measured and modeled in both LCP and FCP were smaller with lower T_a and radiation from late August to early September (Figure 3) than were those measured and modeled from late July to mid-August (Figure 2). CO_2 effluxes measured and modeled during this later period were similar to those earlier. Consequently, lower features in both landforms were only small net C sinks while higher features were net C sources (NEP less than zero) during this period with shorter daylengths. (Figures 3b and 3c). Spatial variation in CO_2 influxes and CH_4 effluxes measured and modeled among features in the LCP and FCP (Figures 3d and 3e) were similar to that earlier in the year, with larger values in lower features than in higher.

4.4. Modeling Spatial Variation in Ecosystem CO_2 and CH_4 Fluxes

Topographic effects on CO_2 influxes and effluxes were modeled in *ecosys* through topographic effects on nutrient availability from surface inputs and soil mineralization. Snow and surface water redistribution from higher to lower features (Grant et al., 2017, Figure 7) transported mineral N in snowpack meltwater and surface runoff from higher to lower features. Wetter soils with deeper snowpacks modeled in lower features caused greater net mineralization by aerobic and anaerobic heterotrophs (A26) than in higher features due to more persistent active layers and warmer soil during autumns and winters (Grant et al., 2017, Figure 6). Greater N transfers and mineralization in lower features contributed to greater root N uptake (C23) and

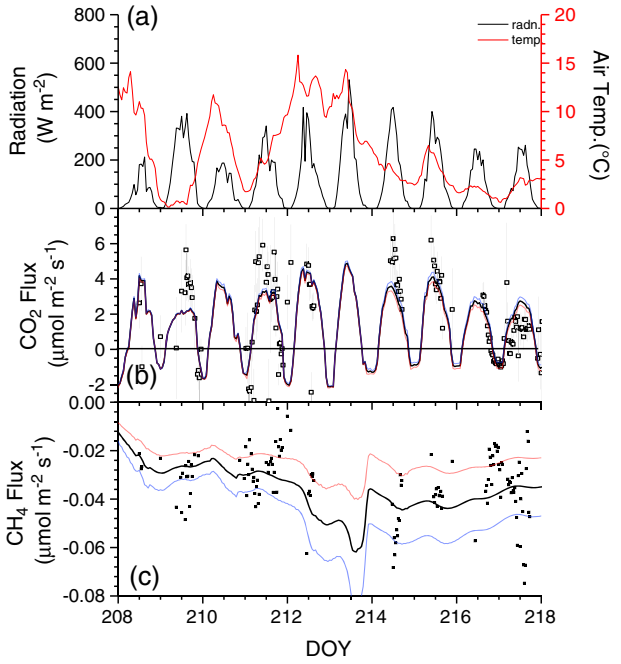

Figure 4. (a) Recorded radiation and temperature, (b) CO_2 fluxes, and (c) CH_4 fluxes modeled in low-centered polygons (light blue lines), flat-centered polygons (light red lines), and spatially averaged fluxes (black lines) for comparison with eddy covariance measurements (symbols) at BEO during late July and early August 2013. Measured fluxes from Torn et al. (2016). For fluxes, positive values indicate influxes, while negative values indicate effluxes.

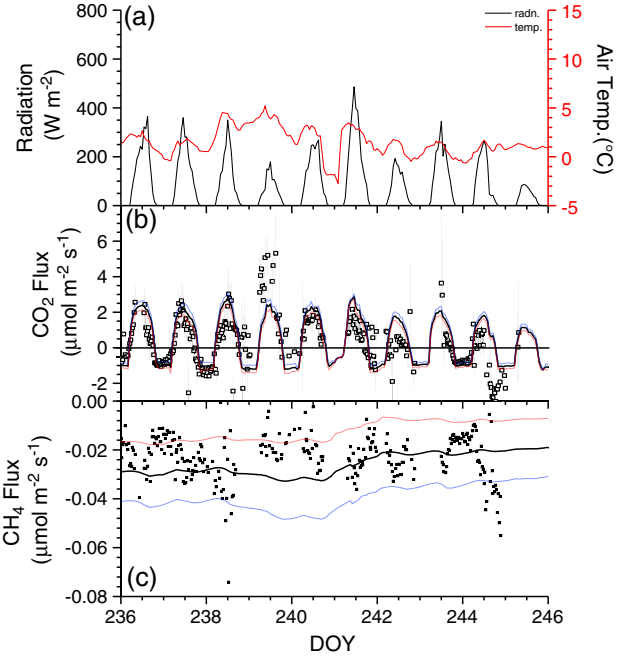

Figure 5. (a) Recorded radiation and temperature, (b) CO_2 fluxes, and (c) CH_4 fluxes modeled in low-centered polygons (light blue lines), flat-centered polygons (light red lines), and spatially averaged fluxes (black lines) for comparison with eddy covariance measurements (symbols) at BEO during late August to early September 2013. Measured fluxes from Torn et al. (2016). For fluxes, positive values indicate influxes, while negative values indicate effluxes.

root to shoot N transfer (C51) to sustain greater canopy CO_2 fixation (C1–C12) (Figures 2b and 2c and 3b and 3c). These model results were consistent with observations at BEO by Wainwright et al. (2015) that CO_2 fluxes were greatest in troughs of all polygon types.

4.5. Seasonal Variation in CO_2 and CH_4 Fluxes Aggregated Over a Polygon Landscape

Modeled CO_2 and CH_4 fluxes aggregated across all features within LCP and FCP landforms were compared with those measured by EC (Figures 4 and 5). Regressions of hourly averaged CO_2 and CH_4 fluxes measured by EC on those modeled over area-weighted LCP and FCP landforms gave intercepts near zero, slopes close to one, and RMSD that was comparable to RMSE (Table 3), indicating no apparent bias in modeled values. The correlation coefficient from the CO_2 regression was smaller than those from earlier model tests in nonpolygonal arctic wetlands (e.g., 0.7–0.8 in Grant et al., 2015), suggesting that spatial variation in fluxes from different polygons within the EC fetch area (e.g., Figures 2 and 3) may have caused some of the variation in EC measurements.

Landscape CO_2 fluxes measured and modeled during 2013 varied seasonally with T_a and radiation. CO_2 influxes and effluxes modeled under peak T_a and radiation in middle to late July (Figure 4a) rose with warming from DOY 209 to 214 and then declined with cooling from DOY 214 to 218 (Figures 4a and 4b). The decline with cooling was also apparent in the measured fluxes, but the confidence with which modeled and measured fluxes could be compared was limited by uncertainty in measured values. However, large influxes measured on some cooler days (e.g., DOY 210) were not simulated by the model. CO_2 influxes modeled over the LCP were slightly larger than those over the FCP (Figure 4b) due to larger influxes modeled in LCP features (Figures 2b and 2c).

Modeled CH_4 effluxes also rose with warming from DOY 209 to 214 and then declined slightly with cooling from DOY 214 to 218 (Figure 4c), although no trends were apparent in measured effluxes. Effluxes modeled over the LCP were larger than those over the FCP due to larger effluxes modeled in LCP features (Figures 2d and 2e). Differences between effluxes modeled in the LCP and FCP accounted for most of the range in effluxes measured by EC over the polygonal landscape.

Modeled and measured CO_2 and CH_4 fluxes were also compared during late August under lower T_a and radiation (Figure 5a). Modeled CO_2 influxes and effluxes declined gradually with cooling from DOY 240 to 246 (Figure 5b). Measured fluxes followed a similar trend, although the confidence with which modeled and measured values could be compared continued to be limited by uncertainty in measured values. CO_2 influxes modeled and measured over the polygonal landscape during late August were smaller than those during late July (Figure 5b versus Figure 4b) when both T_a and radiation were greater (Figure 5a versus Figure 4a), as were CO_2 influxes modeled at troughs, rims, and centers within the landscape (Figures 3b and 3c versus Figures 2b and 2c). However, CO_2 effluxes modeled and measured during late August remained similar to those during late July, as did those at troughs, rims, and centers within the landscape, because late-season declines in soil temperatures (T_s) driving R_h and below-ground R_a

Table 3
Statistics From Regressions of Hourly Averaged CO_2 and CH_4 Fluxes Measured by Eddy Covariance (Torn et al., 2016) on Those Modeled Over Combined LCP and HCP Landforms at BEO During 2013

Flux	a[a]	b[a]	R^2	RMSD[b]	RMSE[c]	n
	μmol m^{-2} s^{-1}			μmol m^{-2} s^{-1}	μmol m^{-2} s^{-1}	
CO_2	0.22	0.83	0.46*	1.39	1.1	843
CH_4	0.00	0.91	0.51*	0.01	not determined	856

[a]$Y = a + bX$ from regression of measured Y on simulated X. [b]RMSD from regression of measured Y on simulated X.
[c]RMSE estimated from EC measurements by Billesbach (2011).
*Significant at $p < 0.001$.

lagged those in T_a, which drove canopy temperature T_c and hence GPP, indicating a substantial decline in landscape NEP during August.

Modeled CH_4 effluxes also declined slightly with cooling from DOY 240 to 246, although scatter in the EC effluxes did not allow a decline to be inferred from measured values (Figure 5c). However, CH_4 effluxes modeled and measured from the polygonal landscape during late August remained similar to those during late July (Figure 5c versus Figure 4c) as did CO_2 effluxes. Differences between effluxes modeled in the LCP and FCP continued to account for most of the range in effluxes measured by EC over the polygonal landscape.

4.6. Spatial Variation in Annual CO_2 and CH_4 Exchange Among Features Within Polygon Landforms

Annual aggregations of CO_2 and CH_4 fluxes modeled in each feature during 2013 indicated that annual GPP and NPP in lower features (LCP troughs and centers and FCP troughs) were greater than those in higher features (LCP rims and FCP rims and centers) (Table 4). Greater annual NPP in lower features was indicated by greater CO_2 influxes modeled and measured in troughs than in rims (section 4.3; Figures 2b and 2c and 3b and 3c). Annual R_h was smaller in lower features than in higher (Table 4) because R_h modeled during the growing season was reduced in wetter soils with lower $[O_{2s}]$ (Figure 1 and Table 4). Annual R_h was therefore smaller relative to NPP in lower features than in higher, as indicated by CO_2 effluxes that were smaller relative to CO_2 influxes in troughs than in rims (Figures 2b and 2c and 3b and 3c). Consequently, annual NEP of lower features was greater than that of higher features. Greater annual CH_4 emissions were modeled

Table 4
Annual Gross Primary Productivity (GPP), Autotrophic Respiration (R_a), Net Primary Productivity (NPP), Heterotrophic Respiration (R_h), Methane Flux (CH_4), and Net Ecosystem Productivity (NEP) Modeled in Troughs, Rims and Centers of Low- and Flat-Centered Polygons (LCP and FCP) During 2013 at Barrow, AK

		Trough		Rim		Center	
		Sedge	Moss	Sedge	Moss	Sedge	Moss
				g C m^{-2} yr^{-1}			
LCP	GPP	133 ± 10	154 ± 6	53 ± 1	195 ± 4	122 ± 10	174 ± 17
	R_a	−60 ± 4	−66 ± 3	−23 ± 1	−79 ± 2	−55 ± 5	−75 ± 9
	NPP	73 ± 6	88 ± 3	30 ± 1	117 ± 2	67 ± 5	99 ± 8
	R_h:	−103 ± 4		−132 ± 4		−108 ± 2	
	CH_4	−4.4 ± 1.1		−0.1 ± 0.06		−5.7 ± 0.5	
	NEP[a]	54 ± 8		15 ± 4		52 ± 9	
FCP	GPP	128 ± 26	188 ± 29	68 ± 7	188 ± 6	61 ± 2	196 ± 4
	R_a	−56 ± 12	−85 ± 14	−30 ± 3	−78 ± 2	−27 ± 1	−79 ± 1
	NPP	72 ± 14	103 ± 15	39 ± 4	110 ± 4	34 ± 2	117 ± 3
	R_h	−115 ± 4		−151 ± 1		−147 ± 2	
	CH_4	−3.8 ± 0.9		−0.0 ± 0.0		−0.0 ± 0.0	
	NEP[b]	56 ± 6		−2 ± 1		4 ± 4	

Note. Positive values represent downward fluxes, while negative values represent upward fluxes.
[a]1 January to 15 May, 1 September to 31 December. [b]Modeled NEP also includes effluxes of DOC and DIC and changes in stocks of soil DIC not shown here. [c]16 May to 31 August.

Table 5
Vascular Aboveground Biomass and Leaf Area Index (LAI) Modeled and Measured in Low-Centered and Flat-Centered Polygons (LCP and FCP) at BEO on 1–3 August 2012

	Trough		Rim		Center	
	Modeled	Measured	Modeled	Measured	Modeled	Measured
	Aboveground biomass (g C m^{-2})					
LCP	51.9 ± 4.3	41.0 ± 10.9	21.9 ± 0.7	21.0 ± 14.4	48.1 ± 4.1	28.5 ± 8.2
FCP	49.4 ± 9.8	39.9 ± 9.3	27.8 ± 2.6	11.4 ± 3.8	25.7 ± 0.7	24.7 ± 9.9
	LAI (m^2 m^{-2})					
LCP	0.60 ± 0.03	0.83 ± 0.20	0.32 ± 0.01	0.33 ± 0.24	0.59 ± 0.04	0.51 ± 0.17
FCP	0.60 ± 0.09	0.72 ± 0.17	0.40 ± 0.03	0.15 ± 0.05	0.37 ± 0.01	0.29 ± 0.11

Note. Modeled uncertainties represent SD of values modeled in all grid cells of each feature.

in lower features than in higher (Table 4), particularly in the LCP, consistent with greater CH_4 fluxes measured and modeled during the growing season (Figures 2d and 2e and 3d and 3e).

Feature elevation also affected the distribution of PFTs in the model. GPP and NPP modeled in higher features were dominated by moss while those in lower were more evenly partitioned between sedge and moss (Table 4). Greater sedge NPP modeled in lower features caused aboveground biomass and LAI of sedge to be larger than those modeled in higher features (Table 5). Aboveground biomass and LAI of sedge measured in lower features were also larger than those in higher, particularly in the FCP (Table 5). However, biomass of sedge modeled in LCP centers was similar to those in LCP troughs, while those measured were smaller, consistent with CO_2 influxes modeled in the LCP center that were greater than those measured during the growing season (Figures 2b and 3b).

4.7. Modeling Spatial Variation in Annual CO_2 and CH_4 Exchange

Modeled topographic effects on water, $[O_{2s}]$, and nutrient availability affected annual CO_2 exchange and CH_4 emissions by altering growth of sedge versus moss PFTs (Table 4). In lower features, periods with standing surface water occurred when water inputs from later and more rapid melt of deeper snowpacks in spring (Grant et al., 2017, Figure 7), and from precipitation events during summer, exceeded runoff and drainage (D1). During these periods, low $[O_{2s}]$ adversely affected near-surface nutrient uptake and hence CO_2 fixation by moss but not by sedge, which maintained root R_a and hence nutrient uptake by direct transfer of atmospheric O_2 into porous roots (D14b and D16d). This transfer conferred a competitive advantage on sedge during these periods that enabled greater sedge productivity and growth in lower features (Tables 4 and 5). In higher features with earlier and slower melt from shallower snowpacks and with more rapid runoff and drainage of surface water, standing water and hence low $[O_{2s}]$ rarely occurred. The absence of standing water allowed more rapid moss growth that increased nutrient competition with sedge and hence adversely affected sedge productivity and growth in higher features. Although moss acquired some N from biological fixation (F12) (Grant et al., 2015), it also competed with sedge for soil mineral N, as has been observed in a wide range of ecosystems (Ayres et al., 2006). The greater dominance of moss modeled in higher features reduced ecosystem CO_2 influxes (Figures 2b and 2c) and annual GPP (Table 4) because C and nutrient cycling were slowed by lower moss N content and hence CO_2 fixation capacity, and by more recalcitrant moss litter and hence slower mineralization.

Differences in modeled productivity of sedge versus moss among landform features were consistent with observations at BEO by Wainwright et al. (2015) that sedges typically fill wet troughs and centers of LCPs, while mosses and lichens usually dominate drier rims of LCPs and centers of FCPs. Model results for sedge and moss productivity were also consistent with observations at BEO by Wainwright et al. (2015) that vegetation density was greater in LCPs than in other polygons. Greater sedge productivity in lower features caused greater NPP relative to growing season R_h, increasing NEP modeled in lower features from those in higher features (Table 4). These model results were consistent with observations that lower lying and hence wetter topographic positions tend to be CO_2 sinks while more elevated and hence drier positions tend to be CO_2 sources during growing seasons in arctic landscapes (Sjögersten et al., 2006).

Greater sedge productivity in lower features also caused increases in modeled CH_4 emissions by transfer of aqueous CH_4 from anaerobic soil (G7 and G12) to porous sedge roots that drove volatilization to gaseous

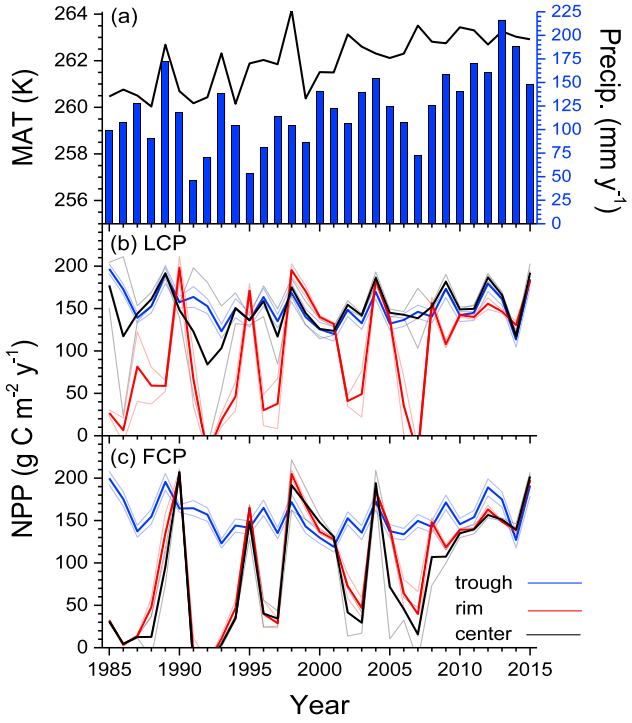

Figure 6. (a) Mean annual temperature (line) and annual precipitation (bars) at Barrow, AK, from Xu and Yuan (2016) for 1985 to 15 June 2013 and from Hinzman et al. (2016) thereafter, and net primary productivity (NPP) modeled (lines) in troughs, rims, and centers of the (b) LCP and (c) FCP. The lighter lines indicate standard deviation of values modeled for all grid cells in each feature.

CH_4 in aerenchyma (D14b) and hence transfer through aerenchyma to the atmosphere (D16d), thereby avoiding methanotrophy in aerobic surface soil (G18). Consequently, CH_4 emissions increased with sedge growth as modeled in earlier studies (Grant, 2015) and observed in meta-analyses of arctic CH_4 emissions (Olefeldt et al., 2013). Model results were consistent with observations at BEO by Wainwright et al. (2015) that CH_4 emissions were significantly greater in LCPs than in FCPs for all polygon features, with no significant emissions in the centers or rims of FCPs.

4.8. Interannual Variation in GHG Exchange and Productivity Among Features Within Polygon Landforms

Weather data from 1981 to 2015 for Barrow AK derived by Xu and Yuan (2016) and recorded by Hinzman et al. (2016) indicated gradually rising MAT (0.1°C yr^{-1}, $P < 0.001$) and precipitation (1.9 mm yr^{-1}, $P = 0.002$) (Figure 6a). Productivity and GHG exchange modeled under historically average MAT and precipitation, represented by repeating 1987 weather, remained stable in all features of the LCP and FCP from 1985 to 2015, indicating that the model had achieved biological equilibrium under the site conditions at Barrow within the first 5 years of the model runs. Interannual variation in productivity and GHG exchange modeled from 1985 to 2015 (Figures 6b and 6c, 7b and 7c, and 8b and 8c) could therefore be attributed to that in the weather data for Barrow.

During this period, NPP modeled in LCP troughs and centers averaged 148 g C m^{-2} yr^{-1} with interannual variation of ±24 g C m^{-2} yr^{-1} (Figure 6b). NPP modeled in LCP rims averaged 99 g C m^{-2} yr^{-1} with a large interannual variation of ±67 g C m^{-2} yr^{-1}. The large interannual variation in rim NPP was attributed mostly to that in moss NPP, which declined sharply with drying and rose sharply with wetting. Smaller NPP was modeled in LCP rims following winters during which snowfall was insufficient for snowpacks to accumulate after redistribution to adjacent troughs and centers (Grant et al., 2017). Greater NPP was modeled in LCP rims when water stress was avoided with soil wetting from greater precipitation and/or snowmelt (e.g., 2004 and 2008–2015) or following warmer years with greater ALD (e.g., 1990 and 1999) (Grant et al., 2017). A similar spatial pattern of interannual variation in NPP was modeled in the FCP, except that lower NPP was also modeled in the FCP centers (Figure 6c), which were particularly vulnerable to soil drying (Grant et al., 2017, Figure 3b). In both modeled landforms, sustained increases in precipitation and ALD from 2008 to 2015 (Grant et al., 2017) caused sustained increases in NPP of higher features. Increases in NPP were associated with increases in ALD in all land features (Table 6a).

Interannual variation in modeled NPP was greater than that in R_h, largely because R_h was less sensitive to soil drying in higher features than was NPP, so that interannual variation in NEP modeled from 1985 to 2015 followed that in NPP (Figures 7b and 7c). NEP modeled in lower features averaged 18 ± 22 g C m^{-2} yr^{-1}, indicating a consistent C sink, while NEP modeled in higher features averaged 12 ± 49 g C m^{-2} yr^{-1}, indicating a smaller C sink with large interannual variation.

Interannual variation in CH_4 emissions modeled in lower features from 1985 to 2015 was associated with that in MAT and precipitation. Emissions rose during years with greater MAT (1989) and precipitation (2000 and 2004) and declined during years with lower MAT (1990, 1991, and 1999) and precipitation (1990, 1991, 1999, 2006, and 2007). About 30%–40% of these emissions were modeled between 15 September and 15 May so that annual emissions in the model would be greater than estimates of emissions derived from growing season measurements. Emissions modeled in higher features remained smaller than those in lower, consistent with smaller CH_4 fluxes measured and modeled in higher features during 2013 (Figures 2 and 3). Because MAT and precipitation affected ALD (Grant et al., 2017, Table 5), interannual variation in annual CH_4 emissions modeled from 1985 to 2015 was associated with that in ALD for most landform features (Table 6b).

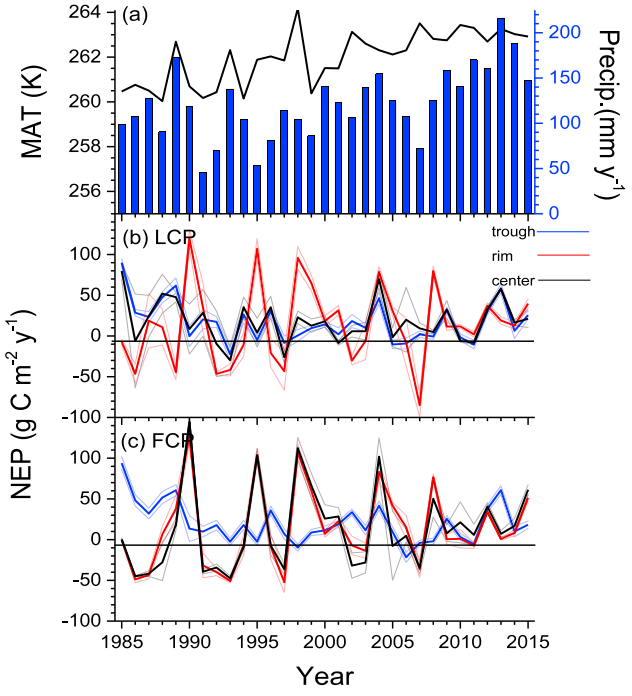

Figure 7. (a) Mean annual temperature (line) and annual precipitation (bars) at Barrow, AK, from Xu and Yuan (2016) for 1985 to 15 June 2013 and from Hinzman et al. (2016) thereafter, and net ecosystem productivity (NEP) modeled (lines) in troughs, rims, and centers of the (b) LCP and (c) FCP. The lighter lines indicate standard deviation of values modeled for all grid cells in each feature.

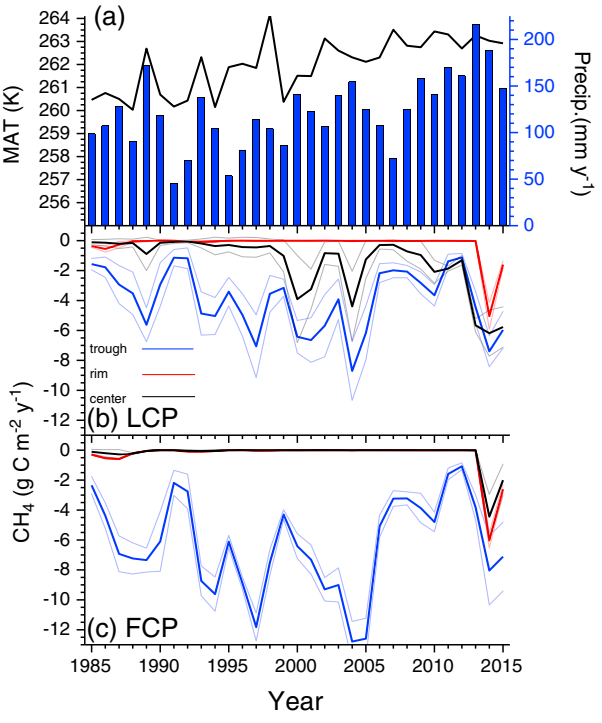

Figure 8. (a) Mean annual temperature (line) and annual precipitation (bars) at Barrow, AK, from Xu and Yuan (2016) for 1985 to 15 June 2013 and from Hinzman et al. (2016) thereafter, and methane emissions (CH_4) modeled (lines) in troughs, rims, and centers of the (b) LCP and (c) FCP. The lighter lines indicate standard deviation of values modeled for all grid cells in each feature.

4.9. Modeling Interannual Variation in GHG Exchange and Productivity

Spatially averaged annual NPP modeled in both the LCP and FCP from 1985 to 2015 was similar to values from 89 to 132 g C m^{-2} yr^{-1} estimated from repeated biomass harvests in different wet sedge tundras at Barrow by Miller et al. (1980). Increases in NPP modeled in lower features during years with greater ALD (1989, 1998, 2004, and 2012) were attributed to increases in sedge NPP sustained by increases in NH_4^+ uptake (C23) with growth of deeper, porous roots (C20b) coupled with increases in NH_4^+ mineralization (A26) in deeper and more persistent active layers. However, N uptake by shallow moss mycorrhizae varied little with ALD, as did N_2 fixation in moss canopies (F12), and hence, interannual variation of moss NPP in lower features was less than that of sedge. Increases in NPP modeled in higher features during and following years with greater ALD (1990, 1998, 2004, and 2009–2015) were attributed to soil wetting from increased recharge with greater ALD (Grant et al., 2017). The consequent correlations of NPP with ALD both spatially (Table 4) and temporally (Table 6a) in the model was consistent with the findings of Dafflon et al. (2017) at BEO that remotely sensed indices of plant productivity showed significant positive correlations with thaw depth.

Sharp declines in NPP were modeled in higher features during years when losses of water from evapotranspiration (Grant et al., 2017, Figure 4) and redistribution of snow and surface water to adjacent lower features (Grant et al., 2017, Figure 3) exceeded gains of water from precipitation and recharge. Smaller snowpacks during winters reduced or eliminated soil wetting of rims from snowmelt, causing water stress which delayed plant growth in spring. Consequent soil drying reduced modeled NPP by reducing soil water potential (ψ_s) and increasing soil hydraulic resistance, thereby forcing lower canopy water potential (ψ_c) in moss and sedge, and higher canopy stomatal resistance (r_c) in sedge, when equilibrating soil water uptake through roots or rhizoids with transpiration from canopies (B14). Lower ψ_c in both moss and sedge, and higher r_c in sedge, forced slower CO_2 fixation with soil drying (Grant & Flanagan, 2007) (C4, C6, and C7), which reduced growth during the growing season and replenishment of plant nonstructural C reserves during autumn. Several such years in succession caused depletion of these reserves, which slowed subsequent leafout and growth (e.g., 1991–1994 in Figure 6a). Drying effects on productivity were particularly strong in moss, which lacked stomatal control of transpiration, and had access only to near-surface water because of limited rhizoid depth (Dimitrov et al., 2011). Consequently, moss NPP modeled in higher features declined more with soil drying and increased more with soil wetting than did sedge NPP, contributing to the large interannual variability of NPP modeled in these features.

Declines in moss and sedge NPP and consequent increases in litterfall (C18) modeled during drier years in higher features caused surface litter accumulation that corresponded to observations of greater dead plant material on dry centers in polygonal landforms at BEO (Wainwright et al., 2015). The greater area of more productive lower features modeled in the LCP versus FCP caused aggregated NPP of the LCP to be greater than that of the FCP (Figure 6b versus Figure 6c), consistent

Table 6
Correlations of Annual (a) NPP and (b) CH_4 Emissions With Active Layer Depth (ALD) Modeled on 31 August at Barrow, AK, From 1985 to 2014

	ALD	
Feature	R^2	P
(a) NPP	**LCP**	
Troughs	0.17	0.013
Centers	0.27	0.001
Rims	0.27	0.001
	FCP	
Troughs	0.31	<0.001
Centers	0.22	0.004
Rims	0.30	<0.001
(b) CH_4	**LCP**	
Troughs	0.17	0.013
Centers	0.52	<0.001
Rims	0.23	0.003
	FCP	
Troughs	0.05	not significant
Centers	0.49	<0.001
Rims	0.34	<0.001

with observations of greater vegetation density in LCPs than in other landforms at BEO by Wainwright et al. (2015). However, sustained increases in NPP modeled in higher features with increases in precipitation from 2008 to 2015 indicated that greening of polygonal landforms with projected increases in precipitation during the next century (Bintanja & Selten, 2014) may be most apparent as greater moss density in higher features, particularly in FCPs and HCPs.

Annual CH_4 emissions modeled from 1985 to 2015 (Figure 8b) were in a range similar to one of 2.7 to 6.2 g C m^{-2} yr^{-1} estimated from 1999 to 2003 at Barrow from measurements by Harazono et al. (2006). Increases in CH_4 emissions modeled with increases in ALD and precipitation in lower, but not in higher, features from 1985 to 2012 (Table 6b and Figures 8b and 8c) were consistent with observations that seasonal CH_4 emissions increased with thaw depth and precipitation in lower, but not in upper, positions in other poorly drained ecosystems in permafrost zones (Iwata et al., 2015; Yu et al., 2017). However, increases in ALD modeled with warming and wetting of LCP centers after 1999, and of all higher features after 2008 (Grant et al., 2017, Figure 8), eventually caused increases in CH_4 emissions to be modeled in these features after 2012 (Figures 8b and 8c). These modeled increases indicate that projected rises in precipitation during the next century (Bintanja & Selten, 2014) may hasten increases in CH_4 emissions from centers of LCPs and from higher features of LCPs and FCPs in polygonal tundra.

In the model, these increases in CH_4 emissions with ALD were attributed to slightly warmer soil that hastened R_h and below-ground R_a and hence microbial and root O_2 demand (A16 and C14) and that reduced O_2 solubility and hence slowed O_2 supply (A14). Increased demand and reduced supply combined to reduce (O_{2s}) and thereby to hasten fermentation (G1) and methanogenesis (G7 and G12) in an anaerobic soil volume that increased with ALD. Increases in CH_4 emissions with ALD and precipitation were also attributed to more rapid early sedge growth that increased root density and hence CH_4 transport to the atmosphere through porous sedge roots (D16d). Each of these attributions was small in itself, but combined to generate large interannual variation characteristic of CH_4 emissions.

5. Summary

1. Topographic effects on CO_2 fluxes caused lower features to be net C sinks and higher features to be near C neutral.
2. Topographic effects on CH_4 fluxes caused lower features to be larger CH_4 sources and higher features to be smaller CH_4 sources.
3. Much of the spatial and temporal variations in CO_2 and CH_4 fluxes were attributed in the model to topographic effects of water and snow movement on θ and thereby on ALD and aqueous O_2 concentrations within the active layer.
4. Model results forced with meteorological data from 1981 to 2014 indicated gradually increasing ALD, with increasing NPP in higher features and CH_4 emissions in some lower and higher features since 2008, attributed mostly to recent rises in temperature and precipitation.
5. The large temporal variation in NEP and CH_4 emissions modeled and measured in different features of the LCP and FCP indicated that landform features and interannual variation in weather need to be represented in models used to project climate change effects on GHG exchange in polygonal tundra.
6. The modeled responses of NPP and CH_4 emissions to precipitation indicate that increases in precipitation projected during the next century may cause substantial increases of NPP in higher features and of CH_4 emissions in some lower and higher features.

Acknowledgments
This research was supported by the Director, Office of Science, Office of Biological and Environmental Research of the U.S. Department of Energy under contract DE-AC02-05CH11231 to Lawrence Berkeley National Laboratory as part of the Next-Generation Ecosystem Experiments in the Arctic (NGEE-Arctic) project. Data used in this paper are available from the NGEE website as cited in the text.

References

Ayres, E., van der Wal, R., Sommerkorn, M., & Bardgett, R. D. (2006). Direct uptake of soil nitrogen by mosses. *Biology Letters*, *2*, 286–288. https://doi.org/10.1098/rsbl.2006.0455

Billesbach, D. P. (2011). Estimating uncertainties in individual eddy covariance flux measurements: A comparison of methods and a proposed new method. *Agricultural and Forest Meteorology*, *151*, 394–405. https://doi.org/10.1016/j.agrformet.2010.12.001

Bintanja, R., & Selten, F. M. (2014). Future increases in Arctic precipitation linked to local evaporation and sea-ice retreat. *Nature*, *509*(7501), 479–482. https://doi.org/10.1038/nature13259

Dafflon, B., Hubbard, S., Ulrich, C., Peterson, J., Wu, Y., Wainwright, H., & Kneafsey, T. J. (2016). Geophysical estimation of shallow permafrost distribution and properties in an ice-wedge polygon-dominated Arctic tundra region. *Geophysics*, *81*(1), WA247–WA263. https://doi.org/10.1190/geo2015-0175.1

Dafflon, B., Oktem, R., Peterson, J., Ulrich, C., Tran, A. P., Romanovsky, V., & Hubbard, S. S. (2017). Coincident aboveground and belowground autonomous monitoring to quantify covariability in permafrost, soil, and vegetation properties in Arctic tundra. *Journal of Geophysical Research: Biogeosciences*, *122*, 1321–1342. https://doi.org/10.1002/2016JG003724

Dimitrov, D. D., Bhatti, J. S., & Grant, R. F. (2014). The transition zones (ecotone) between boreal forests and peatlands: Ecological controls on ecosystem productivity along a transition zone between upland black spruce forest and a poor forested fen in central Saskatchewan. *Ecological Modelling*, *291*, 96–108. https://doi.org/10.1016/j.ecolmodel.2014.07.020

Dimitrov, D. D., Grant, R. F., LaFleur, P. M., & Humphreys, E. (2011). Modelling the effects of hydrology on gross primary productivity and net ecosystem productivity at Mer Bleue bog. *Journal of Geophysical Research: Biogeosciences*, *116*, G04010. https://doi.org/10.1029/2010JG001586

Grant, R. F. (2015). Ecosystem CO_2 and CH_4 exchange in a mixed tundra and a fen within a hydrologically diverse Arctic landscape. Part II. Modelled impacts of climate change. *Journal of Geophysical Research: Biogeosciences*, *120*, 1388–1406. https://doi.org/10.1002/2014JG002889

Grant, R. F., Desai, A., & Sulman, B. (2012). Modelling contrasting responses of wetland productivity to changes in water table depth. *Biogeosciences*, *9*, 4215–4231. https://doi.org/10.5194/bg-9-4215-2012

Grant, R. F., & Flanagan, L. B. (2007). Modeling stomatal and nonstomatal effects of water deficits on CO_2 fixation in a semiarid grassland. *Journal of Geophysical Research*, *112*, G03011. https://doi.org/10.1029/2006JG000302

Grant, R. F., Humphreys, E. R., & Lafleur, P. M. (2015). Ecosystem CO_2 and CH_4 exchange in a mixed tundra and a fen within a hydrologically diverse Arctic landscape. Part I. Modelling vs. measurements. *Journal of Geophysical Research: Biogeosciences*, *120*, 1366–1387. https://doi.org/10.1002/2014JG002888

Grant, R. F., Mekonnen, Z. A., Riley, W. J., Wainwright, H. M., Graham, D., & Torn, M. S. (2017). Mathematical modelling of arctic polygonal tundra with *ecosys*: 1. Microtopography determines how active layer depths respond to changes in temperature and precipitation. *Journal of Geophysical Research: Biogeosciences*, *122*, 3161–3173. https://doi.org/10.1002/2017JG004035

Grant, R. F., & Roulet, N. T. (2002). Methane efflux form boreal wetlands: Theory and testing of the ecosystem model *ecosys* with chamber and tower flux measurements, *Global Biogeochemical Cycles*, *16*(4), 1054. https://doi.org/10.1029/2001GB001702

Harazono, Y., Mano, M., Miyata, A., Yoshimoto, M., Zulueta, R. C., Vourlitis, G. L., … Oechel, W. C. (2006). Temporal and spatial differences of methane flux at arctic tundra in Alaska. *Memoirs of National Institute of Polar Research Special Issue*, *59*, 79–95.

Hinzman, L., Romanovsky, V., Cable, W., & Busey, G. (2016). Surface meteorology, Barrow, Alaska, Area A, B, C and D, ongoing from 2012. Retrieved from: http://ngee-arctic.ornl.gov/. accessed 19 January 2016

Iwata, H., Harazono, Y., Ueyama, M., Sakabe, A., Nagano, H., Kosugi, Y., … Kim, Y. (2015). Methane exchange in a poorly-drained black spruce forest over permafrost observed using the eddy covariance technique. *Agricultural and Forest Meteorology*, *214-215*, 157–168. https://doi.org/10.1016/j.agrformet.2015.08.252

Kumar, J., Collier, N., Bisht, G., Mills, R. T., Thornton, P. E., Iversen, C. M., & Romanovsky, V. (2016). Modeling the spatiotemporal variability in subsurface thermal regimes across a low-relief polygonal tundra landscape. *The Cryosphere*, *10*(5), 2241–2274. https://doi.org/10.5194/tc-10-2241-2016

Mezbahuddin, M., Grant, R. F., & Hirano, T. (2014). Modelling effects of seasonal variation in water table depth on net ecosystem CO_2 exchange of a tropical peatland. *Biogeosciences*, *11*(3), 577–599. https://doi.org/10.5194/bg-11-577-2014

Miller, P. C., Webber, P. J., Oechel, W. C., & Tieszen, L. L. (1980). Biophysical processes and primary production. In J. Brown, et al. (Eds.), *An arctic ecosystem: The coastal tundra at Barrow, Alaska*, *US/IBP Synthesis Series* (Vol. 12, pp. 66–101). Stroudsberg, PA: Dowden, Hutchison and Ross, Inc.

Morrissey, L. A., & Livingston, G. P. (1992). Methane flux from tundra ecosystems in arctic Alaska: An assessment of local spatial variability. *Journal of Geophysical Research*, *97*(D15), 16,661–16,670. https://doi.org/10.1029/92JD00063

Olefeldt, D., Turetsky, M. R., Crill, P. M., & Mcguire, A. D. (2013). Environmental and physical controls on northern terrestrial methane emissions across permafrost zones. *Global Change Biology*, *19*(2), 589–603. https://doi.org/10.1111/gcb.12071

Olivas, P. C., Oberbauer, S. F., Tweedie, C. E., Oechel, W. C., Lin, D., & Kuchy, A. (2011). Effects of fine-scale topography on CO_2 flux components of Alaskan coastal plain tundra: Response to contrasting growing seasons. *Arctic, Antarctic, and Alpine Research*, *43*, 256–266. https://doi.org/10.1657/1938-4246-43.2.256

Shiklomanov, N. I., Streletskiy, D. A., Nelson, F. E., Hollister, R. D., Romanovsky, V. E., Tweedie, C. E., … Brown, J. (2010). Decadal variations of active-layer thickness in moisture-controlled landscapes, Barrow, Alaska. *Journal of Geophysical Research*, *115*, G00I04. https://doi.org/10.1029/2009JG001248

Sjögersten, S., van der Wal, R., & Woodin, S. J. (2006). Small-scale hydrological variation determines landscape CO_2 fluxes in the high Arctic. *Biogeochemistry*, *80*, 205–216. https://doi.org/10.1007/s10533-006-9018-6

Sommerkorn, M. (2008). Micro-topographic patterns unravel controls of soil water and temperature on soil respiration in three Siberian tundra systems. *Soil Biology and Biochemistry*, *40*, 1792–1802. https://doi.org/10.1016/j.soilbio.2008.03.002

Torn, M. S. (2016). CO_2 CH_4 flux air temperature soil temperature and soil moisture, Barrow, Alaska 2013 ver. 1. Retrieved from: http://ngee-arctic.ornl.gov/. accessed 5.June.2016

Torn, M., Raz-Yaseef, N., & Billesbach, D. (2016). Eddy-covariance and auxiliary measurements, NGEE-Barrow, 2012–2013. Retrieved from: http://ngee-arctic.ornl.gov/. accessed 5.June.2016

Vaughn, L. J. S., Conrad, M. E., Bill, M., & Torn, M. S. (2016). Isotopic insights into methane production, oxidation, and emissions in Arctic polygon tundra. *Global Change Biology*, *22*(10), 3487–3502. https://doi.org/10.1111/gcb.13281

Wainwright, H. M., Dafflon, B., Smith, L. J., Hahn, M. S., Curtis, J. B., Wu, Y., … Hubbard, S. S. (2015). Identifying multiscale zonation and assessing the relative importance of polygon geomorphology on carbon fluxes in an Arctic tundra ecosystem. *Journal of Geophysical Research: Biogeosciences*, *120*, 788–808. https://doi.org/10.1002/2014JG002799

Xu, X., & Yuan, F. (2016). Meteorological forcing at Barrow AK 1981–2013. Retrieved from http://ngee-arctic.ornl.gov/. accessed 22 June 2016

Yu, X. Y., Song, C. C., Sun, L., Wang, X. W., Shi, F. X., Cui, Q., & Tan, W. W. (2017). Growing season methane emissions from a permafrost peatland of northeast China: Observations using open-path eddy covariance method. *Atmospheric Environment*, *153*, 135–149. https://doi.org/10.1016/j.atmosenv.2017.01.026

Zona, D., Lipson, D. A., Zulueta, R. C., Oberbauer, S. F., & Oechel, W. C. (2011). Microtopographic controls on ecosystem functioning in the Arctic coastal plain. *Journal of Geophysical Research*, *116*, G00I08. https://doi.org/10.1029/2009JG001241

Zona, D., Oechel, W. C., Kochendorfer, J., Paw U, K. T., Salyuk, A. N., Olivas, P. C., … Lipson, D. A. (2009). Methane fluxes during the initiation of a large-scale water table manipulation experiment in the Alaskan Arctic tundra. *Global Biogeochemical Cycles*, *23*, GB2013. https://doi.org/10.1029/2009GB003487